

Crystal Structure, Stability and Li Superionic Conductivity of Pyrochlore-Type Solid Electrolyte $\text{Li}_{2-x}\text{La}_{(1+x)/3}\text{Nb}_2\text{O}_6\text{F}$: A First-Principles Calculation Study

Randy Jalem,^{1,*} Kazunori Takada,¹ Hitoshi Onodera², and Shuhei Yoshida²

¹Center for Green Research on Energy and Environmental Materials (GREEN), National Institute for Materials Science (NIMS), 1-1 Namiki, Tsukuba, Ibaraki 305-0044, Japan

²Environment Neutral System Development Division, DENSO CORPORATION, 1 Yoshiike, Kusagi, Agui-cho, Chita-gun, Aichi 470-2298, Japan

Email: JALEM.Randy@nims.go.jp

Abstract

Recently, a new oxide-type solid electrolyte (SE) for all-solid-state Li ion batteries, pyrochlore-type $\text{Li}_{2-x}\text{La}_{(1+x)/3}\text{Nb}_2\text{O}_6\text{F}$ (LLNOF), was reported to exhibit Li^+ superionic conductivity of 3.9×10^{-3} S/cm at room temperature. To gain understanding on this novel SE, in this work, thermodynamic analysis and *ab initio* molecular dynamics (AIMD) calculations based on the density functional theory (DFT) framework were performed to clarify the material's phase stability, electrochemical stability and Li^+ ion transport property. LLNOF is predicted to be a metastable phase and thus, its electrochemical window is likely to be determined by its decomposition phases. The Li transport pathway is revealed to be defined by the large hexagonal tunnels formed by corner-sharing NbO_6 units, these tunnels can either be La-free or La-blocked depending on the Li/La/vacancy configuration. The Li^+ ion conduction mechanism proceeds in a concerted migration manner in the $16d$ sites via an intermediate site. Analysis of phonon density of states shows that F atoms have a lower phonon-energy band center position than O atoms, this is correlated with the characteristically low phonon-energy band center position of Li atoms and the observed Li^+ superionic conductivity of LLNOF.

Introduction

A solid electrolyte (SE) with Li superionic conductivity is one of the key materials that is needed to finally unlock the full commercialization of all-solid-state Li-ion batteries (ASSBs). So far, a number of SE classes have been reported, each with its own merits and demerits.¹⁻³ One class is sulfide-type SEs which are known for demonstrating Li superionic conductivity at room temperature ($\sigma_{\text{Li,RT}}$), notable ones include $\alpha\text{-Li}_3\text{PS}_4$ (1.3×10^{-3} S/cm)⁴ and $\text{Li}_{9.54}\text{Si}_{1.74}\text{P}_{1.44}\text{S}_{11.7}\text{Cl}_{0.3}$ (2.5×10^{-2} S/cm)⁵. However, sulfide-type SEs generally suffer from issues of chemical reactivity with air moisture, resulting to the generation of toxic H_2S gas.⁶ Another class is the oxide-type SEs are intrinsically very stable in air, some of the reported materials in this SE class with relatively high conductivity belong to Li-based garnet oxides,⁷⁻⁹ specifically the cubic $\text{Li}_7\text{La}_3\text{Zr}_2\text{O}_{12}$ (LLZO) which shows a conductivity of up to 1×10^{-3} S/cm via appropriate cation doping¹⁰. Although such degree of conductivity can be considered high, it still falls short relative to sulfide-type SEs with respect to the practical-level design

requirement (10^{-2} S/cm or higher) which is necessary to reduce the overall battery cell impedance down to $< 40 \Omega\text{cm}^2$ and achieve $> 250 \text{ Wh/kg}$ in usable capacity.¹¹

Recently, a new oxide-type SE, the pyrochlore-type $\text{Li}_{2-x}\text{La}_{(1+x)/3}\text{Nb}_2\text{O}_6\text{F}$ (LLNOF) was reported to show a total $\sigma_{\text{Li,RT}}$ of $3.9 \times 10^{-3} \text{ S/cm}$.¹² Its crystal structure has a cubic symmetry ($Fd\bar{3}m$, Figure 1a) and is characterized by NbO_6 octahedral units (16c Nb and 48f O) forming large hexagonal tunnels (Fig. 1b). In the tunnels, there are two Wyckoff sites: a partially occupied 16d site for Li/La/Vacancies (Vac) and the 8b site for F anions. Li/La cations form pseudo-rhombohedral units with O and F anions as vertices (i.e., LiO_6F_2 , LaO_6F_2 ; Fig. 1c). The Li pathway channels are effectively determined by the tunnels which can be either La-free or La-blocked, depending on the actual La site occupancy/position (Fig. 1d). Along the tunnels, the F-Li/La-F linkage assumes a zigzag pattern (Fig. S1). From a Li-center viewpoint, the two F atoms are located at the *trans*-position vertices of the LiO_6F_2 unit. From a F-center viewpoint, previous ^{19}F MAS NMR spectroscopy results reveal six different environments for F atoms in a fourfold coordination with Li/La/Vac species.¹³

In this work, DFT and AIMD calculations were employed to study the LLNOF's phase stability, electrochemical stability, and Li^+ ion transport property. The Li pathway network and connectivity within the structure were investigated using geometric-based Voronoi-tessellation algorithm and 3D percolation theory approach. The Li^+ ion dynamics and element-specific vibrational properties were analyzed using the van Hove space-time correlation technique and the Fourier transform of the velocity autocorrelation function, respectively, using the AIMD trajectory data. Our findings offer useful insights for the rational design of SEs for ASSB application.

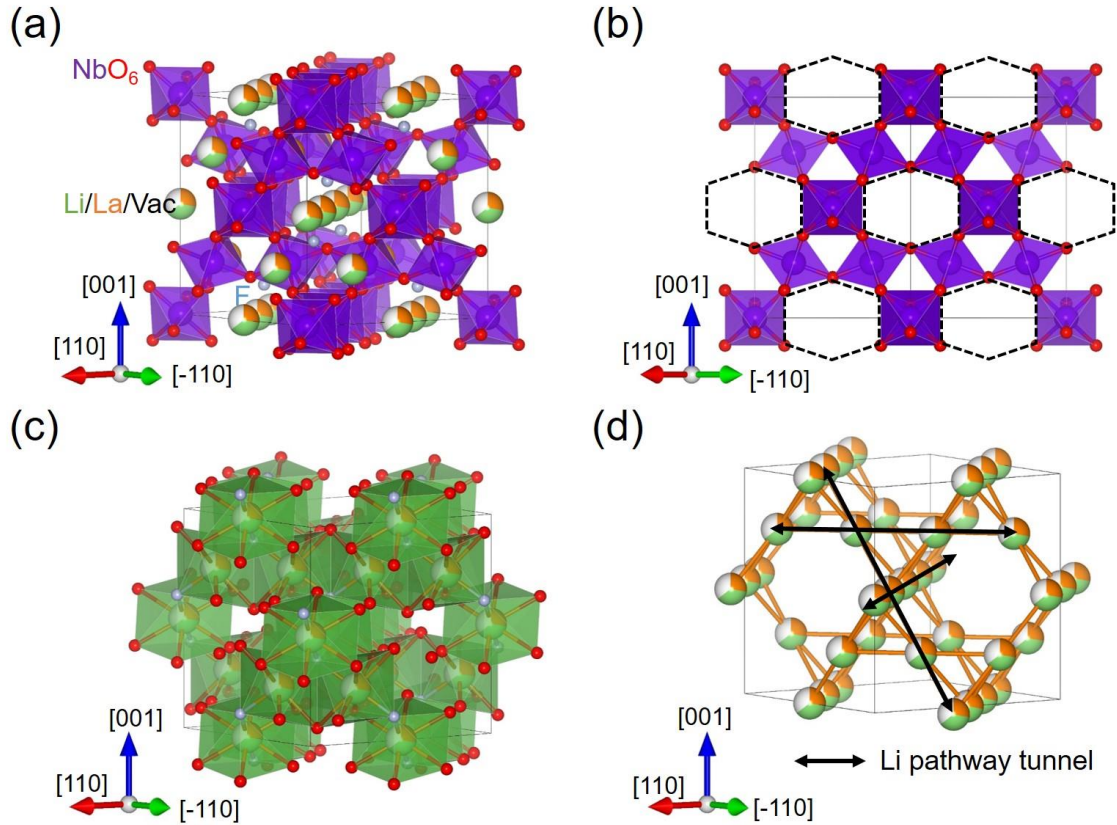


Figure 1. Crystal structure of $Fd\bar{3}m$ $\text{Li}_{2-x}\text{La}_{(1+x)/3}\text{Nb}_2\text{O}_6\text{F}$ which is expanded by a supercell matrix $[[1\ 1\ 0], [-1\ 1\ 0], [0\ 0\ 1]]$: (a) 3D perspective view of corner-sharing NbO_6 octahedral units and isolated $\text{Li/La/Vacancy(Vac)}$ species, (b) NbO_6 -characterized hexagonal tunnels (dashed lines) where Li , La , and F atoms occupy, (c) edge-sharing $\text{Li/LaO}_6\text{F}_2$ pseudo-rhombohedral units, and (d) linkages of partially occupied $16d$ sites for Li/La/Vac species which also determine the Li pathway channels; double-headed arrows highlight intersecting tunnels defined by $16d$ sites.

Computational details

The Vienna *Ab Initio* Simulation Package (VASP), which employs the generalized gradient approximation (GGA) approach and the projector augmented wave (PAW) method basis set, was used for DFT calculations.¹⁴⁻¹⁵ The initial LLNOF structure data is provided in Table S1. To allow for a richer sampling of Li/La/Vac configurations, the unit cell was expanded using a supercell matrix $[[1,1,0], [-1,1,0], [0,0,1]]$. In this model size, the closest composition with respect to experiment ($\text{Li}_{1.25}\text{La}_{0.58}\text{Nb}_2\text{O}_6\text{F}$) is $x = 0.6875$ or $\text{Li}_{1.3125}\text{La}_{0.5625}\text{Nb}_2\text{O}_6\text{F}$ (174-atoms supercell). For phase stability analysis, other compositions/structures were also considered (i.e., $x = [0.5, 0.875, 1.0625, 1.25]$). For a given composition, a total of 1,000 Li/La/Vac arrangements were randomly generated and sorted based on the electrostatic Ewald energy (E_{Ewald}) criterion. E_{Ewald} calculations were performed using the pymatgen code.¹⁶ From this step, 10 lowest- E_{Ewald} structures were picked and subjected to

DFT structure relaxation. The lowest DFT total-energy structure was then used for thermodynamic and ion dynamics analyses, unless otherwise specified. The kinetic energy cutoff was set to 520 eV and the k-point grid (with the Monkhorst-Pack grid scheme) was fixed to at least 1000.¹⁷ Li with semicore s states as valence states, standard La, Nb with semicore s states as valence states, standard O, and standard F were used as pseudopotentials. Convergence conditions were set to <1 meV/atom and <0.01 eV/Å in energy and residual force, respectively.

The thermodynamic phase stability of LLNOF as a function of Li/La content was evaluated using the convex hull method. A Gibbs free energy (G) model within the Li-La-Nb-O-F system was constructed as follows:¹⁸

$$G(T, P, N_{Li}, N_{La}, N_{Nb}, N_{O_2}, N_F) = E(T, P, N_{Li}, N_{La}, N_{Nb}, N_{O_2}, N_F) + PV(T, P, N_{Li}, N_{La}, N_{Nb}, N_{O_2}, N_F) - TS(T, P, N_{Li}, N_{La}, N_{Nb}, N_{O_2}, N_F), \quad (1)$$

where E is formation energy, PV is the energy term to account for pressure effects, and TS for system entropy by temperature effect. At normal pressure condition, $P\Delta V$ contribution was assumed to be negligible. Similarly, at room temperature condition, $T\Delta S$ contribution was also considered to be small and thus was excluded as well. Therefore, equation (1) can be simplified by constructing a 0-K phase diagram and by taking the convex hull of 0-K formation energy data for all the relevant phases. The thermodynamic decomposition energy (E_d) is given by:

$$E_d = E(c) - E(\text{LLNOF}), \quad (2)$$

where $E(c)$ and $E(\text{LLNOF})$ are the convex hull energies using formation enthalpy data, relative to the phase equilibria at composition c of ground-state phases corresponding to LLNOF stoichiometry. For the construction of the Li-La-Nb-O-F phase diagram, the DFT total energies of relevant phases were taken from experimental compounds from Inorganic Crystal Structure Database (ICSD) and from *in-silico* compound entries of Materials Project database, respectively.^{16, 19-20}

For electrochemical stability evaluation, the grand potential phase diagram was constructed for the LLNOF SE, with the electrostatic potential (ϕ) considered in the definition of Li chemical potential (μ_{Li}):²¹

$$\mu_{Li}(\phi) = \mu_{Li}^{ref} - e\phi, \quad (3)$$

where μ_{Li}^{ref} is the reference chemical potential based on Li metal. The decomposition reaction energy for the ϕ -specific decomposition reactions can be calculated as follows:

$$E_d(\phi) = E(c, \phi) - E(\text{LLNOF}) - \Delta n_{Li} \mu_{Li}(\phi), \quad (4)$$

where $E(c, \phi)$ is the phase equilibria energy at composition c and ϕ , while Δn_{Li} denotes the change of the number of Li between LLNOF and phase equilibria at composition c .

For AIMD calculations, the kinetic energy cutoff was set to 400 eV and the k-point was fixed to $1 \times 1 \times 1$. Standard pseudopotentials were used for all elements. The MD step size was set to 1 fs. Atomic trajectory sampling was carried out at different MD temperatures: 600 K, 800 K, 1000 K, 1200 K, and 1400 K. To account for thermal expansion effects, a 20,000-steps MD equilibration procedure was

initially performed using a Langevin thermostat (NPT ensemble) at each target MD temperature,²² then the average lattice parameters to be used for each MD temperature were estimated by averaging the lattice cell information from the last 5,000 MD steps of the equilibration step. The MD production run was set with a trajectory length of 100,000 steps, using a Nosé–Hoover thermostat (NVT ensemble).²³

Statistical observables were estimated by mean squared displacement (*MSD*) analysis:²⁴

$$MSD = \langle [\vec{r}(t + \tau) - \vec{r}(t)]^2 \rangle, \quad (5)$$

where $\vec{r}(t)$ and τ Li⁺ ion position at time t and lag time, respectively.

The Li diffusion coefficient (D_{Li}) was determined by the following equation:²⁵

$$D_{Li} = \lim_{t \rightarrow \infty} [\langle [\vec{r}(t + \tau) - \vec{r}(t)]^2 \rangle / 2dt] \quad (6)$$

where d represents Li⁺ ion diffusion dimensionality.

The Li⁺ ion conductivity (σ_{Li}) was calculated based on Nernst-Einstein relationship:²⁶

$$\sigma_{Li} = \rho F^2 z_{Li}^2 D_{Li} / RT, \quad (7)$$

where ρ , F , z_{Li} , R , and T are Li⁺ ion mass density, Faraday constant, Li⁺ ion charge, gas constant, and temperature, respectively.

For ion dynamics and correlation analysis, the van Hove space-time correlation function (G) was used:²⁷

$$G(\vec{r}, t) = \langle \sum_{i=1}^N \delta(\vec{r} + \vec{r}_i(0) - \vec{r}_i(t)) \rangle / N + \langle \sum_{i \neq j}^N \delta(\vec{r} + \vec{r}_j(0) - \vec{r}_i(t)) \rangle / N, \quad (8)$$

where $\langle \cdot \rangle$ and $\delta(\cdot)$ are ensemble-averaged quantities and 3D Dirac delta function, respectively. The first and second term account for the Li self-correlation ($G_s(\vec{r}, t)$) and distinct Li-Li correlation ($G_d(\vec{r}, t)$), respectively.

Experimental details

Information on material synthesis and characterization by cyclic voltammetry are available in the Supporting Information section.

Results and Discussion

Structure configuration and phase stability

Fig. 2a shows the E_{Ewald} distribution of 1,000 LLNOF structures with randomly sampled Li/La/Vac ordering. It has a positively skewed distribution in the range of -41.35 to -40.74 eV/atom with a median value of $\tilde{E}_{Ewald} = -41.19$ eV/atom. High- E_{Ewald} structures are noted to have locally clustered La^{3+} cations while low- E_{Ewald} structures have a relatively more homogeneous Li/La/Vac arrangements with no 1st-nearest-neighbor (1NN) La^{3+} - La^{3+} pairs within the characteristic hexagonal tunnels. It is noted that in ionic materials, electrostatic interaction contributes dominantly to the DFT total energy (E_0) (i.e., low- E_{Ewald} structures generally tends to have low E_0). Based on this correlation between E_{Ewald} and E_0 , the E_{Ewald} ordering of different structure configurations can be exploited to cheaply find potentially low- E_0 structures such as in the Li/La/Vac ordering in LLNOF. The configuration with the lowest DFT total-energy (E_0) out of the 10 lowest- E_{Ewald} structures, as displayed in Fig. 2b, is chosen as the representative LLNOF structure (L1: index number 6, $E_0 = -7.999$ eV/atom). This structure has two La-free tunnels (Fig. 2c), with the rest of its tunnels being La-blocked. On the other hand, the other structures which have a slightly higher E_0 relative to LLNOF-L1 have only one La-free tunnel, as shown in Fig. 2d (M1: index number 1, $E_0 = -7.983$ eV/atom). It is noted that number of La-free/blocked tunnels is also composition-specific. However, the sample E_0 values lie in a narrow range of ~ 24 meV/atom, so room-temperature entropic effects (~ 30 meV/atom) may facilitate for the phase stabilization of structures with more La-blocked tunnels than the L1 structure (e.g., via appropriate quenching/annealing procedure from high temperature during synthesis²⁸).

The thermodynamic phase stability of LLNOF as a function of Li/La content is shown in Table 1. Over the series composition, all phases are predicted to be metastable (i.e., $E_d > 0$), with a generally increasing stability (i.e., decreasing E_d) with decreasing (increasing) Li (La) content. Thus, the experimental LLNOF composition (i.e., $\text{Li}_{1.25}\text{La}_{0.58}\text{Nb}_2\text{O}_6\text{F}$), which is within the investigated composition range in $\text{Li}_{2-x}\text{La}_{(1+x)/3}\text{Nb}_2\text{O}_6\text{F}$ (i.e., $x = [0.5, 0.6875, 0.875, 1.0625, 1.25]$), is highly likely to be a metastable phase as well. The calculated E_d values for the sampled configurations in Fig. 2b, including the representative structures in Table 1, are found to be within the predicted limit of metastability for experimental-database oxides.²⁹

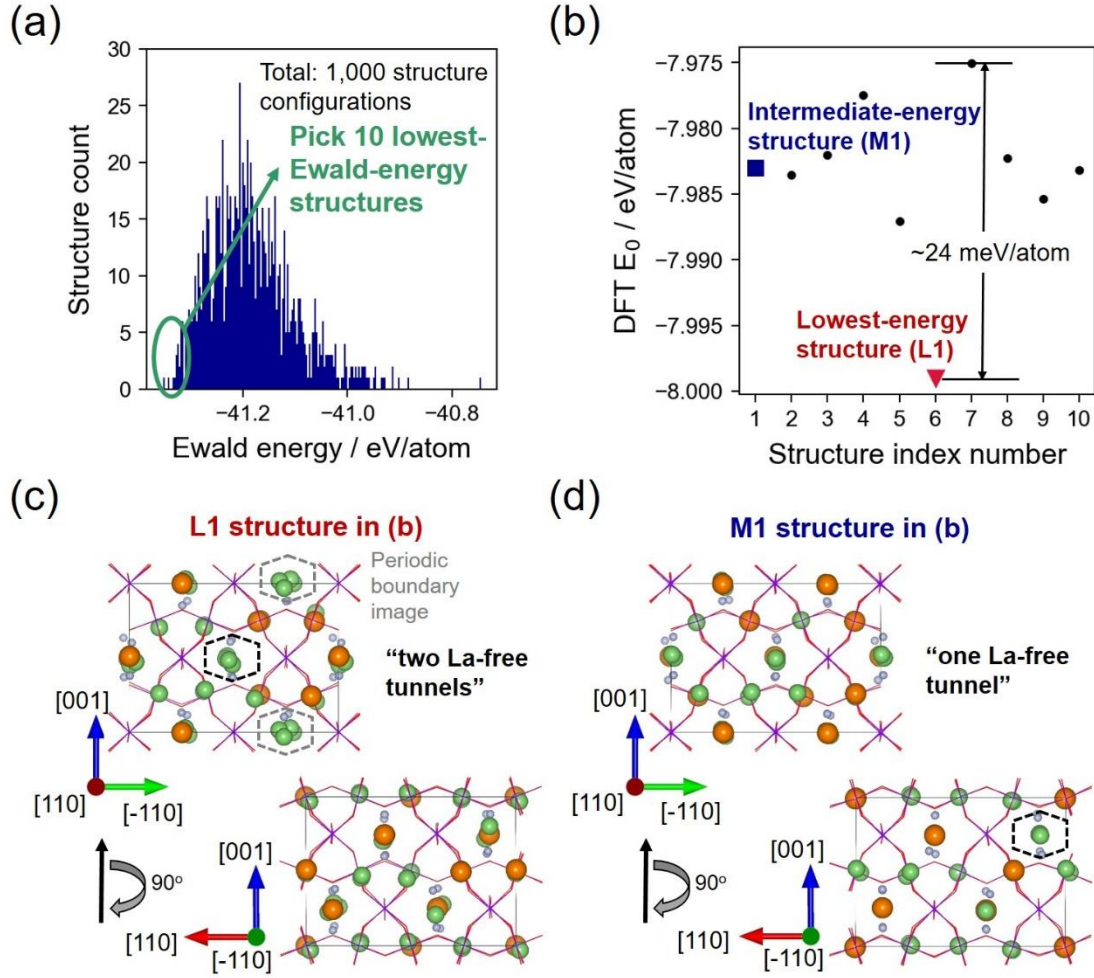


Figure 2. (a) Ewald energy (E_{Ewald}) distribution plot for randomly sampled Li/La/Vac ordering in the $\text{Li}_{1.3125}\text{La}_{0.5625}\text{Nb}_2\text{O}_6\text{F}$ model composition with 32 ordering sites in its 174-atoms supercell. (b) DFT total energies (E_0) of 10 lowest- E_{Ewald} structures that are picked in (a). (c) Lowest- E_0 structure (L1: structure index number 6 in (b)) characterized by two La-free tunnels (bounding dashed line). (d) Intermediate- E_0 structure (M1: structure index number 1 in (b)) characterized by one La-free tunnel. Li, La, and F atoms are shown as green, orange, and light blue spheres, respectively, while NbO_6 units are displayed as wireframes.

Table 1. DFT decomposition energies (E_d) and products of $\text{Li}_{2-x}\text{La}_{(1+x)/3}\text{Nb}_2\text{O}_6\text{F}$ (LLNOF) phases.

x	Supercell formula	Reduced formula	E_d / meV/atom	Decomposition products
0.5	$\text{Li}_{24}\text{La}_8\text{Nb}_{32}\text{O}_{96}\text{F}_{16}$	$\text{Li}_{1.5}\text{La}_{0.5}\text{Nb}_2\text{O}_6\text{F}$	50	LiNb_3O_8 , LaNbO_4 , LiF
0.6875*	$\text{Li}_{21}\text{La}_9\text{Nb}_{32}\text{O}_{96}\text{F}_{16}$	$\text{Li}_{1.3125}\text{La}_{0.5625}\text{Nb}_2\text{O}_6\text{F}$	31	LiNb_3O_8 , LaNbO_4 , Nb_2O_5 , LiF
0.875	$\text{Li}_{18}\text{La}_{10}\text{Nb}_{32}\text{O}_{96}\text{F}_{16}$	$\text{Li}_{1.125}\text{La}_{0.625}\text{Nb}_2\text{O}_6\text{F}$	35	LiNb_3O_8 , LaNbO_4 , Nb_2O_5 , LiF
1.0625	$\text{Li}_{15}\text{La}_{11}\text{Nb}_{32}\text{O}_{96}\text{F}_{16}$	$\text{Li}_{0.9375}\text{La}_{0.6875}\text{Nb}_2\text{O}_6\text{F}$	30	LaNbO_4 , Nb_2O_5 , LaF_3 , LiF
1.25	$\text{Li}_{12}\text{La}_{12}\text{Nb}_{32}\text{O}_{96}\text{F}_{16}$	$\text{Li}_{0.75}\text{La}_{0.75}\text{Nb}_2\text{O}_6\text{F}$	23	LaNbO_4 , Nb_2O_5 , LaF_3 , LiF

*Closest model composition to experiment (i.e., $\text{Li}_{1.25}\text{La}_{0.58}\text{Nb}_2\text{O}_6\text{F}$), with the LLNOF-L1 structure as the representative structure (see Fig.2).

Formation of intrinsic bulk defects

Using the $\text{Li}_{1.3125}\text{La}_{0.5625}\text{Nb}_2\text{O}_6\text{F}$ structure (supercell formula: $\text{Li}_{21}\text{La}_9\text{Nb}_{32}\text{O}_{96}\text{F}_{16}$, L1 structure) as the reference structure, the most energetically accessible defect types as shown in Table 2 are LiF Schottky and Li-La antisite defects. The structures with these defects have E_D values that are comparable or lower than the reference structure, indicating that their formation is energetically comparable to that of the reference structure. In the case of LiF Schottky defect which can be represented as x in $\text{Li}_{21-x}\text{La}_9\text{Nb}_{32}\text{O}_{96}\text{F}_{16-x}$ supercell composition (i.e., as reference), E_D does not increase significantly for $x \leq 4$ but it sharply increases for $x > 4$ (Fig. S6). These results suggest that the experimentally synthesized LLNOF may contain F vacancies, aside from Li vacancies. In the case of Li-La antisite defects, it can be readily explained by the intrinsic Li-La disordering at the $16d$ Wyckoff site.

Other defect types that are predicted to be energetically accessible during high-temperature synthesis (< 2 eV per formula unit) are Li Frenkel, La Frenkel, O Frenkel, F Frenkel and O-F antisite defects. Meanwhile, the most energetically unfavorable defect types are Nb Frenkel, Li_2O Schottky, Li-Nb antisite and La-Nb antisite defects. The latter defects have large energy cost for formation due to the unsatisfied coordination environment preference (e.g., Nb^{5+} prefers to stay in an octahedral site), large ion size difference at the substitution site (e.g., $r(\text{La}^{3+}) = 1.16 \text{ \AA}$ vs. $r(\text{Nb}^{5+}) = 0.74 \text{ \AA}$ for an octahedral coordination), and significant local repulsion which can cause large structure distortion (e.g., $\text{Nb}^{5+}\text{-Nb}^{5+}\text{-Nb}^{5+}$ as compared to $\text{Nb}^{5+}\text{-La}^{3+}\text{-Nb}^{5+}$ or $\text{Nb}^{5+}\text{-Li}^+\text{-Nb}^{5+}$ arrangement).

Table 2. DFT-calculated intrinsic bulk defects in $\text{Li}_{1.3125}\text{La}_{0.5625}\text{Nb}_2\text{O}_6\text{F}$ (L1 structure).

Kröger-Vink reaction equation	E_{defect} / eV per formula unit
Li Frenkel: $\text{Li}_{\text{Li}}^{\times} \rightarrow \square'_{\text{Li}} + \text{Li}_{\text{int}}^{\bullet}$	0.86
La Frenkel: $\text{La}_{\text{La}}^{\times} \rightarrow \square'''_{\text{La}} + \text{La}_{\text{int}}^{\bullet\bullet\bullet}$	1.26
Nb Frenkel: $\text{Nb}_{\text{Nb}}^{\times} \rightarrow \square''''_{\text{Nb}} + \text{Nb}_{\text{int}}^{\bullet\bullet\bullet\bullet}$	2.53
O Frenkel: $\text{O}_{\text{O}}^{\times} \rightarrow \square^{\bullet\bullet}_{\text{O}} + \text{O}_{\text{int}}''$	1.08
F Frenkel: $\text{F}_{\text{F}}^{\times} \rightarrow \square^{\bullet}_{\text{F}} + \text{F}_{\text{int}}'$	1.90
LiF Schottky*: $\text{Li}_{\text{Li}}^{\times} + \text{F}_{\text{F}}^{\times} \rightarrow \square'_{\text{Li}} + \square^{\bullet}_{\text{F}} + \text{LiF}$	-
Li_2O Schottky: $2\text{Li}_{\text{Li}}^{\times} + \text{O}_{\text{O}}^{\times} \rightarrow 2\square'_{\text{Li}} + \square^{\bullet}_{\text{O}} + \text{Li}_2\text{O}$	2.46
Li-La antisite*: $\text{Li}_{\text{Li}}^{\times} + \text{La}_{\text{La}}^{\times} \rightarrow \text{La}_{\text{Li}}^{\bullet\bullet} + \text{Li}_{\text{La}}''$	-
Li-Nb antisite: $\text{Li}_{\text{Li}}^{\times} + \text{Nb}_{\text{Nb}}^{\times} \rightarrow \text{Nb}_{\text{Li}}^{\bullet\bullet\bullet\bullet} + \text{Li}_{\text{Nb}}''''$	2.66
La-Nb antisite: $\text{La}_{\text{La}}^{\times} + \text{Nb}_{\text{Nb}}^{\times} \rightarrow \text{Nb}_{\text{La}}^{\bullet\bullet} + \text{La}_{\text{Nb}}''$	2.99
O-F antisite: $\text{O}_{\text{O}}^{\times} + \text{F}_{\text{F}}^{\times} \rightarrow \text{F}_{\text{O}}^{\bullet} + \text{O}_{\text{F}}'$	1.77

* E_{D} is comparable or lower than the reference structure, indicating that the formation of such defective structures is energetically comparable to that of the reference structure.

Electrochemical stability

Here, the phase equilibria at different voltages are used to evaluate the electrochemical window of LLNOF. The stability voltage window based on DFT-based Li grand potential phase diagram analysis is displayed in Fig. 3a; the detailed decomposition reactions are provided in Table S2. As a kinetically stabilized phase, LLNOF in itself has a narrow stability window of 2.49 – 3.92 V (at zero Li uptake/removal). At the low voltage regime, reductive decomposition proceeds, such as at 2.35 V that turns LLNOF into LiNb_3O_8 , $\text{Nb}_{12}\text{O}_{29}$, LaNbO_4 and LiF. This is consistent with the cyclic voltammetry results as shown in Fig. S2, in which the reduction current is observed from around 2 V. At the high voltage regime (> 3.92 V), oxidative reactions that ultimately result to O_2 gas release becomes favorable. Meanwhile, the thermodynamic decomposition phases of LLNOF (i.e., LiNb_3O_8 , LaNbO_4 , Nb_2O_5 , and LiF) may become the effective phases that determine the extent of stability voltage window (i.e., as an interphase-controlled electrochemical window). For Li-containing decomposition phases, LiNb_3O_8 (2.35 – 3.92 V) is shown to have a similar stability voltage window as with LLNOF (Fig. 3b, Table S3), while LiF provides the widest window of 0 – 6.36 V (Fig. 3c, Table S4). The very wide stability window of LiF makes it suitable for suppressing Li dendrite growth.³⁰ LiNb_3O_8 has been reported as a potential anode material for Li^+ ion batteries with $\text{Nb}^{5+}/\text{Nb}^{4+}$ and $\text{Nb}^{4+}/\text{Nb}^{3+}$ redox couples in the 1.0 – 3.0 V range.³¹ This indicates that LiNb_3O_8 can facilitate Li diffusion which may be beneficial for Li ion inter-grain transport. Meanwhile, LLNOF decomposition phases which do not contain Li such as LaNbO_4 and Nb_2O_5 can also have profound impact on battery performance. For LaNbO_4 , further reductive decomposition is predicted at 1.30 V (Table S5), the listed reactions can

result to poor contact at the interface region due to associated volume change, especially with a Li metal anode. Similarly, for Nb₂O₅, further reductive decomposition is also predicted at 2.49 V (see Table S6).

For comparison, the garnet cubic LLZO is also analyzed.⁷ Its voltage window is predicted to be 0.05 – 2.90 V (Fig. 3d, Table S7), suggesting that it has a comparatively lower reduction potential than LLNOF. However, when in direct contact with Li metal (i.e., at 0 V), LLZO is predicted to be unstable. This Li instability has been reported in a previous experimental work.³² Reductive decomposition phases include Li₆Zr₂O₇, Li₂O and La₂O₃. The predicted voltage window of Li₆Zr₂O₇ is 0.05 – 3.21 V (Table S8), suggesting reductive instability vs. Li metal that can promote further decomposition, forming Li₂O as well as species that are associated with Zr⁴⁺ reduction (e.g., Zr₄O, Zr₃O). This decomposition has an associated volume change of -29% based on bulk volumes of Li₆Zr₂O₇, Li metal, Zr₃O, and Li₂O, suggesting a possible contact loss around the electrolyte-anode interface region. Meanwhile, the voltage-specific decomposition analysis of Li₂O (Table S9) reveals stability vs. Li metal, with a window of 0 – 2.90 V. If Li₂O (pre-)exists around solid interface regions (voltage window: 0 – 2.90 V), LLZO reductive stability is possible. However, crystalline Li₂O has a low ionic conductivity ($\sim 10^{-9}$ S/cm) which can result to increased grain boundary resistance.³³ La₂O₃, the other decomposition phase, is also evaluated to be stable vs. Li metal (Table S10), but its lack of energetically favorable Li⁺ ion pathways can also increase the grain boundary resistance. The oxidative potential of both LLZO and Li₂O are lower than LLNOF (3.92 V), which means that the latter should be more stable at the high-voltage regime.

Additional comparative analysis was also performed for garnet-type Li₅La₃Ta₂O₁₂ (LLTO). Based on decomposition energy (E_d) calculation, LLTO is predicted to be a metastable phase ($E_d = 295$ meV/atom), it is thermodynamically driven to decompose into Li₃TaO₄, La₃TaO₇ and La₂O₃ (Table S11); the associated volume change is estimated to be -8%. Li₃TaO₄ is predicted to further decompose at 0.55 V into Li₅TaO₅ and Ta metal (Table S12), the reaction-related volume change is calculated to be -6%. Li₅TaO₅ reductively decomposes into Li₂O and Ta metal at 0.35 V (Table S13), volume change is estimated to be -30%. On the other hand, La₃TaO₇ is shown to reductively decompose below 0.65 V into Li₃TaO₄, La₂O₃, and Ta metal (Table S14), with a volume change of -13%. Overall, the significant volume changes of LLTO decomposition phases are expected to contribute towards particle contact loss in the electrolyte-anode interface.

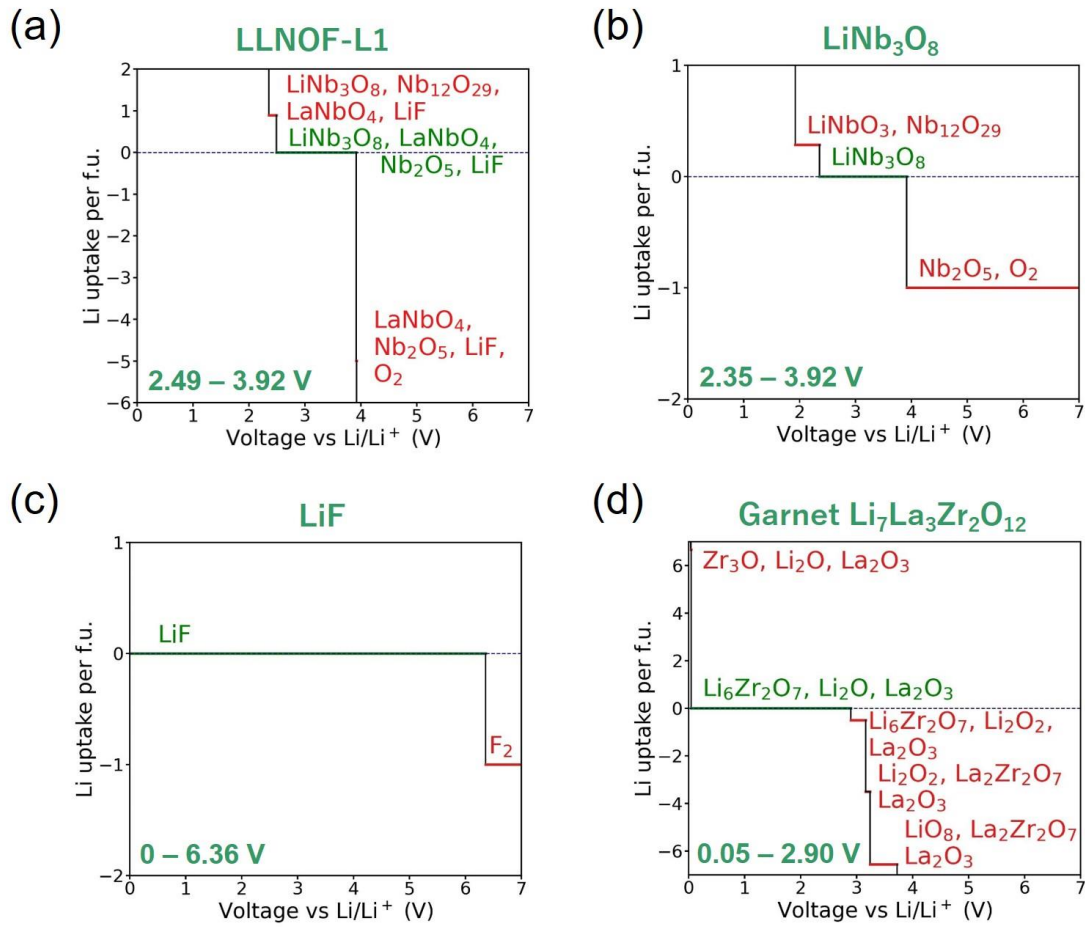


Figure 3. DFT-calculated voltage profile and decomposition by Li grand potential phase diagram analysis upon lithiation and delithiation of (a) pyrochlore-type $\text{Li}_{2-x}\text{La}_{(1+x)/3}\text{Nb}_2\text{O}_6\text{F}$ ($x = 0.6875$) solid electrolyte (SE) and its Li-containing thermodynamic decomposition phases (b) LiNb_3O_8 and (c) LiF . Voltage profile and decomposition for (d) garnet $\text{Li}_7\text{La}_3\text{Zr}_2\text{O}_{12}$ (LLZO) is included for comparison. Stability voltage window (i.e., Li uptake/removal is zero) for each investigated compound functioning as an SE is shown in green. Voltage range and decomposition phases with non-zero Li uptake/removal into/from SE is indicated in red.

Li diffusivity, conductivity

Fig. S3a shows the element-specific *MSD* plots for LLNOF-L1 based on NVT-AIMD production run at 1000 K. Only Li^+ ions are found to be diffusive in the structure according to the observed *MSD* slope, while the other ion types have flat *MSD* profiles (i.e., only vibrational motion). The *MSD* slope increases as the MD temperature increases (Fig. S3b), this is owed to Li ion migration as being a thermally activated process. From the *MSD* slopes, σ_{Li} is calculated and then plotted as a function of temperature; experimental and AIMD data of LLNOF and cubic LLZO SEs are included for comparison (Fig. 4). Statistical observables for LLNOF-L1 and LLNOF-M1 are $[D_{\text{Li},300\text{K}} = 1.87 \times$

10^{-8} cm²/s, $E_a = 0.21$ eV, $\sigma_{\text{Li},300\text{K}} = 1.07 \times 10^{-3}$ S/cm] and [$D_{\text{Li},300\text{K}} = 2.90 \times 10^{-8}$ cm²/s, $E_a = 0.19$ eV, $\sigma_{\text{Li},300\text{K}} = 1.63 \times 10^{-3}$ S/cm], respectively. The predicted bulk $\sigma_{\text{Li},300\text{K}}$ values are in the same order of magnitude vs. reported experimental data. Meanwhile, $\sigma_{\text{Li},300\text{K}}$ shows a slight correlation with the degree Li/La/Vac (dis)ordering. It is evidenced by the ~ 1.5 factor increase in $\sigma_{\text{Li},300\text{K}}$ of the LLNOF-M1 structure (with one La-free tunnel) relative to the LLNOF-L1 structure (with two La-free tunnels).

The Li diffusivity of LLNOF with a given defect type is also investigated, specifically the LiF Schottky defect which is predicted to be one of the most energetically favorable ones (Table 2). The conductivity vs. inverse temperature plot for the LLNOF with one LiF Schottky defect ($x = 1$ in $\text{Li}_{21-x}\text{La}_9\text{Nb}_{32}\text{O}_{96}\text{F}_{16-x}$) is shown above (blue dashed line) shows a ~ 2 orders of magnitude decrease in conductivity relative to the reference LLNOF-L1 structures, the calculated values are 2.02×10^{-5} S/cm ($E_a = 0.36$ eV) vs. 1.07×10^{-3} S/cm ($E_a = 0.21$ eV), respectively.

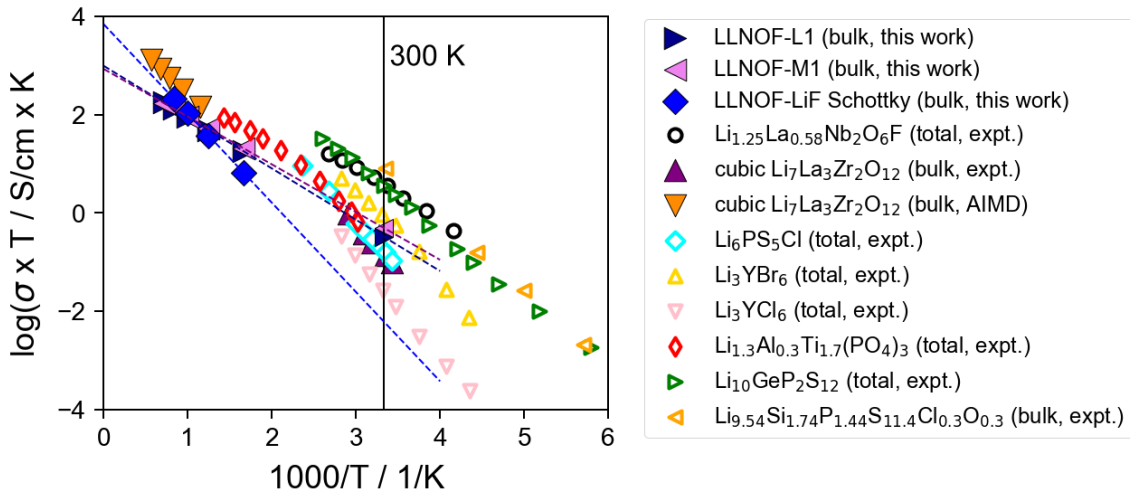


Figure 4. Comparison of the Li^+ ion conductivity of selected all-solid-state battery electrolytes: pyrochlore-type LLNOF-L1 ($\text{Li}_{1.3125}\text{La}_{0.5625}\text{Nb}_2\text{O}_6\text{F}$, Figure 2b), pyrochlore-type LLNOF-M1 ($\text{Li}_{1.3125}\text{La}_{0.5625}\text{Nb}_2\text{O}_6\text{F}$, Figure 2c), experimentally reported LLNOF ($\text{Li}_{1.25}\text{La}_{0.58}\text{Nb}_2\text{O}_6\text{F}$)¹², and cubic $\text{Li}_7\text{La}_3\text{Zr}_2\text{O}_{12}$ solid electrolyte from previous experimental and AIMD-based works^{7, 34}, argyrodite $\text{Li}_6\text{PS}_5\text{Cl}$ experimental total conductivity³⁵, halide Li_3YBr_6 and Li_3YCl_6 ³⁶, Nasicon-type $\text{Li}_{1.3}\text{Al}_{0.3}\text{Ti}_{1.7}(\text{PO}_4)_3$ experimental total conductivity³⁷, $\text{Li}_{10}\text{GeP}_2\text{S}_{12}$ experimental total conductivity³⁸, and $\text{Li}_{9.54}\text{Si}_{1.74}\text{P}_{1.44}\text{S}_{11.4}\text{Cl}_{0.3}\text{O}_{0.3}$ experimental bulk conductivity³⁹.

Li ion transport pathway

The Li transport pathway and connectivity in LLNOF is studied using the 1000-K AIMD trajectory data. Fig. 5a shows the 3D Li trajectory density (red: high, green: intermediate, and blue: low probabilities) within the LLNOF-L1 structure. A contiguous 3D pathway network is visible, indicating

a high degree of accessible local migration routes within the host structure framework. The site-to-site Li^+ ion jump process does not proceed directly through the O-F edge-shared LiO_6F_2 units within the tunnel (i.e., $16d \rightarrow 16d$ transition). Instead, the moving Li^+ ion from a $16d$ site jumps to a neighboring interstitial site to form an “ LiO_6F ” intermediate state, and then it moves to the next-neighbor $16d$ site (i.e., $16d \rightarrow \text{“LiO}_6\text{F”} \rightarrow 16d$ transition) (Fig. 5b). This interstitial site also allows for Li^+ ions to migrate from one tunnel to an intersecting tunnel, and then to a nearby parallel tunnel.

Additionally, it is apparent that the overall pathway topology depends on the Li/La/Vac ordering at the $16d$ sites. When a tunnel is La-blocked (Fig. 5c), the migrating Li^+ ions need to re-route to a tunnel that intersects with its original tunnel in order to achieve long-range transport. The arrangement and proportion of sites occupied by La^{3+} ions can thus affect Li percolation and pathway tortuosity in the LLNOF structure. To quantitatively analyze the extent of this blocking effect, the 3D percolation threshold (p_c) related to the $16d$ sites in LLNOF is evaluated. For this calculation, an expanded cell is used in order to minimize errors related to periodic boundary condition (Fig. S4).⁴⁰ Fig. 5d shows the plot for Li-pathway connectivity (Li + Vac site occupancy fraction) as a function of normalized La content ($f_{\text{La}} = n_{\text{La}}/(n_{\text{Li}} + n_{\text{La}} + n_{\text{Vac}})$). Here, p_c for LLNOF is estimated to be at $f_{\text{La}} = 0.66$, this value is when the Li pathway becomes fully La-occupied (<1% connectivity). It is emphasized that $f_{\text{La}} = 0.66$ is already significantly exceeding the charge neutrality requirement of the $[\text{Nb}_2\text{O}_6\text{F}]^{-3}$ host framework. At relevant compositions such as the LLNOF model composition (i.e., $\text{Li}_{1.3125}\text{La}_{0.5625}\text{Nb}_2\text{O}_6\text{F}$), $f_{\text{La}} = 0.28$ and the site connectivity is ~72% (blue vertical line) which means that there is still sufficient percolation to support long-range bulk Li diffusivity. For the experimentally reported LLNOF composition ($\text{Li}_{1.25}\text{La}_{0.58}\text{Nb}_2\text{O}_6\text{F}$), $f_{\text{La}} = 0.29$ which corresponds to an almost the same degree of connectivity (orange vertical line). At the extreme limit of La substitution that satisfies the charge-neutral condition (i.e., $f_{\text{La}} = 0.5$ or $\text{LaNb}_2\text{O}_6\text{F}$), site connectivity drops to ~46%. In comparison, this composition limit is relatively lower than in the case of progressive Li pathway blocking at the $24d$ tetrahedral and $48g/96h$ octahedral sites in cubic LLZO, which can still retain ~60% site connectivity, such as at the composition limit related to Ga^{3+} blocking.⁴¹ This suggests that the Li pathway in LLNOF is slightly more tortuous than in LLZO.

Analysis on the ion transport pathways in LLNOF were also performed based on a void space characterization technique,⁴²⁻⁴⁶ the resulting interstitial network related to the Li pathways is shown in the Fig. 5e. The 3D channels for the mobile Li^+ ions are successfully identified. The circular cluster of interstice and bottleneck positions labeled as s_1 and s_2 , respectively, can be assigned to positions that are proximate to the $16d$ Wyckoff site (see Fig. 5f). The multiple s_1 positions in the same circular site cluster are energetically according to the corresponding AIMD Li trajectory density in Fig. 5a and 5c. Their symmetric positions also reflect the large intrinsic hexagonal tunnels in the NbO_6F framework of the LLNOF structure. The interstitial network is consistent with the $16d$ - $16d$ transitions for Li^+ ions proceeding via the Li_6OF intermediate state (see Fig. 5b) which also has multiple positions

(see the hexagonal area the Figure below, labeled as i_s); the LiO_6F intermediate state has 4 s_1 positions and 9 s_2 positions. No direct ion jump paths between adjacent $16d$ sites are detected and Li^+ ions move through $16d - i_s - 16d - i_s - 16d - \dots$ path connectivity.

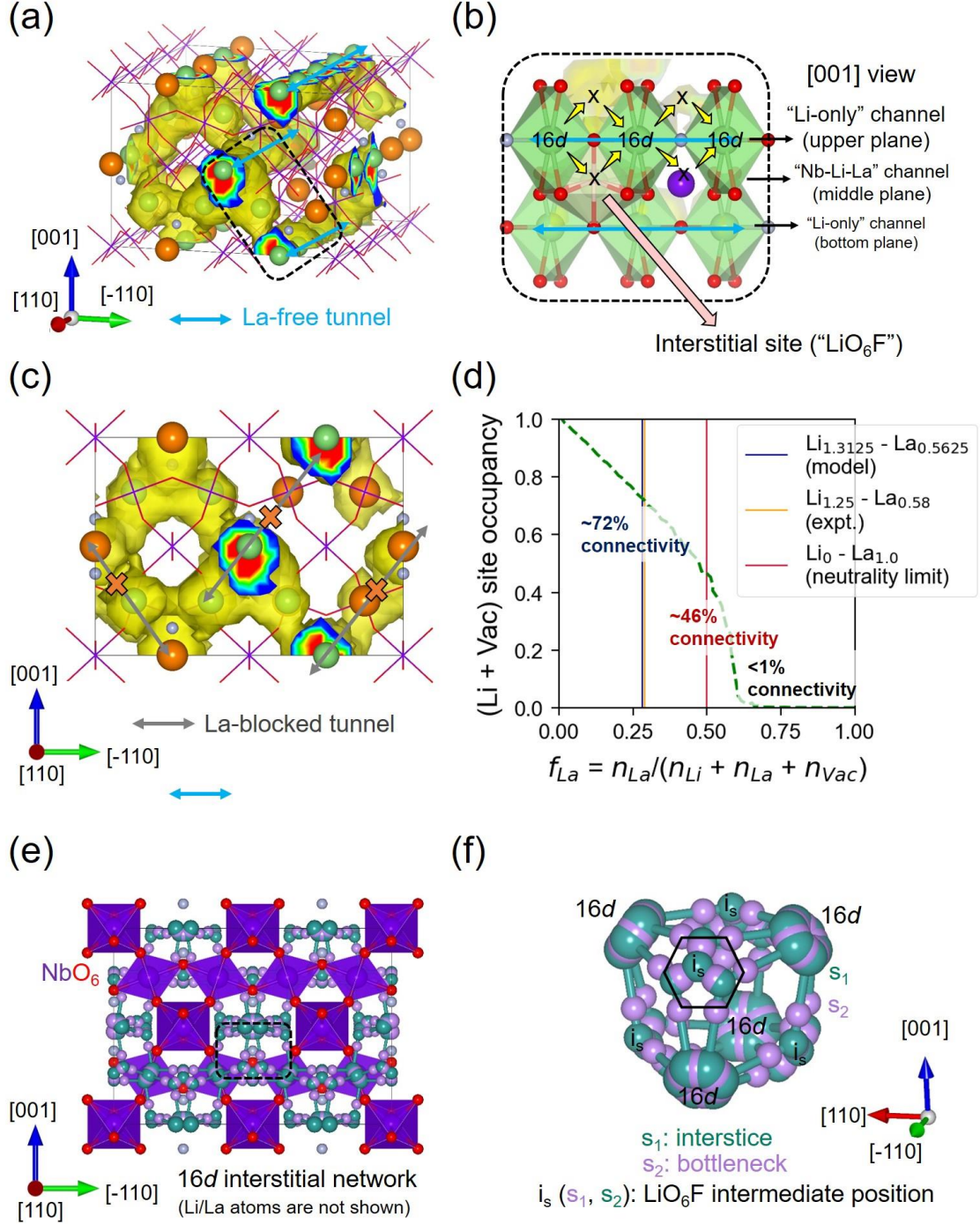


Figure 5. (a) 3D-perspective Li trajectory density within the LLNOF-L1 structure based on 1000-K AIMD calculation. La-free tunnels are indicated as light-blue double-head arrows. NbO₆ units are

displayed in wireframe. (b) A local trajectory density region in (a) is enlarged (dashed-line box) which highlights “Li-only” and “Nb-Li-La” channels and the 16*d* site connectivity for local Li ion migration via interstitial sites (forming “LiO₆F” intermediate state). (c) 2D- view of the Li trajectory density showing La-blocked tunnels as gray double-head arrows. (d) Percolation-based site connectivity fraction (Li + Vac site occupancy) as a function of normalized La content (x), using an expanded LLNOF structure with 32,000 16*d* sites generated by a supercell matrix $[[10, 10, 0], [-10, 10, 0], [0, 0, 10]]$; highlighted compositions are the LLNOF model (Li_{1.3125} – La_{0.5625} or Li_{1.3125}La_{0.5625}Nb₂O₆F), the experimentally reported composition (Li_{1.25} – La_{0.58} or Li_{1.25}La_{0.58}Nb₂O₆F), and La-composition limit for charge neutrality (Li₀ – La_{1.0} or LaNb₂O₆F). A radial distance cutoff of 3.8 Å for site connectivity was employed. (e, f) Interstitial network related to the Li⁺ ion transport pathways obtained from the Nb₂O₆F framework of the pyrochlore LLNOF structure. The network was determined using the void-space analysis technique as described in Ref. 42-46. The circular site cluster can be assigned as proximate to the 16*d* Wyckoff site, while the Li₆O₆F intermediate position is located within the hexagonal area (labeled as *i_s*).

Li⁺ ion conduction mechanism

Fig. 6a shows the heatmap for the self-part $G(r, t)$ (G_s) for Li⁺ ions in the LLNOF-L1 structure, as derived from the 1000-K MD trajectory data; LLZO data is included for comparison (Fig. 6b). By definition, G_s represents the probability distribution of distances traveled by Li⁺ ions. The G_s band center positions correspond to the nearest-neighbor (NN) jump site distances, similar to the local maxima in the Li-Li radial distribution function (RDF, Fig. S5). The G_s band at $r < 2$ Å can be assigned to Li intra-site-cage vibration. The G_s band center positions indicate that Li⁺ ions in LLNOF have a relatively larger average vibrational amplitude than Li⁺ ions in LLZO; $G(r < 2 \text{ Å}, t)$ band center positions are estimated to be ~ 1 Å and ~ 0.5 Å, respectively. As the MD trajectory length increases, Li⁺ ions begin to access positions that are beyond 1st-NN jump sites. For the two SEs, the 1st-NN jump distances are located at $3.5 \text{ Å} < r < 4.5 \text{ Å}$ and $2 \text{ Å} < r < 3 \text{ Å}$, respectively, while the 2nd-NN jump distances lie in the range $5.5 \text{ Å} < r < 8 \text{ Å}$ and $4 \text{ Å} < r < 6 \text{ Å}$, respectively. Clearly, 1st-NN and 2nd-NN jump distances in LLNOF are larger than in LLZO and a similar trend prevails for the 3rd-NN, 4th-NN site jump distances, and so on. Aside from the n^{th} -NN site jump distances, LLNOF and LLZO have different accessible Li positions at intermediate distances according G_s probability buildup at trough-related distances (i.e., between primary bands), the latter distances are located at $r = [\sim 2 \text{ Å}, \sim 5 \text{ Å}, \sim 8 \text{ Å}]$ and $r = [\sim 1.5 \text{ Å}, \sim 3.5 \text{ Å}, \sim 5.5 \text{ Å}, \sim 7.5 \text{ Å}]$, respectively. Collectively, the G_s band center and trough positions have unambiguously differentiated the Li pathway topology network between LLNOF and LLZO.

Fig. 6c and 6d show the G_s heatmap for O²⁻ and F⁻ ions in LLNOF as derived from the 1000-K MD trajectory data. The vibration signature at $r < 2$ Å is prevalent for both anions, with F⁻ ions

demonstrating a relatively larger average vibrational amplitude than O^{2-} ions (i.e., at $r > \sim 1 \text{ \AA}$ vs. at $r < \sim 1 \text{ \AA}$, respectively, see insets). Aside from differences due to atomic mass and electronegativity (i.e., chemical bonding nature) related to F^- and O^{2-} ions, the large space provided by the hexagonal tunnels in LLNOF, wherein F^- and Li^+ ions sit, may have also contributed to the observed large vibration amplitudes. To evaluate this “free space” for vibration, the largest probe sphere diameter (d_0) that can fit inside the hexagonal tunnel network is estimated by 3D Voronoi tessellation analysis of the structure framework (i.e., when all Li atoms are removed).⁴⁷ In LLNOF-L1 and LLNOF-M1, d_0 values are $\sim 2.73 \text{ \AA}$ and $\sim 2.68 \text{ \AA}$, respectively. Interestingly, these values are significantly larger than in LLZO which is only $\sim 1.87 \text{ \AA}$.

Fig. 6e and 6f show the heatmap for the distinct-part $G(r, t)$ (G_d) for Li^+ ions in LLNOF-L1 and LLZO structures, respectively, as determined from 1000-K NVT-MD trajectories. Physically, G_d measures the probability of finding a Li^+ ion at a site (or position) which was formerly vacated by another Li^+ ion. Consequently, it can provide information on concerted ion motion. In both LLNOF and LLZO, the concerted Li ion migration bands are confirmed which are located at $r < 2 \text{ \AA}$ and they persist all throughout the sampled MD trajectory length. The result here on the concerted Li^+ ion migration mechanism in LLZO agrees well with previous theoretical works.^{34, 41, 48} Meanwhile, G_d bands that can be assigned to n^{th} -NN Li jump events are also visible, the distances match well with the peak positions based on Li-Li RDF plots (Fig. S5). However, LLZO exhibits an intermittent G_d signal at $1 \text{ \AA} < r < 2 \text{ \AA}$ which can be assigned to Li rearrangement events related to the accessible off-center positions by Li^+ ions in the $24d$ tetrahedral and the distorted octahedral $48g/96h$ sites.^{7, 34} This Li off-centering is caused by the strong repulsion between Li^+ ions because of geometric frustration related to the 9 available sites per formula unit that need to be populated by 7 Li by stoichiometry and the garnet structure having an intrinsically short Li-Li site distances (e.g., $24d$ -to- $48g$: $\sim 1.99 \text{ \AA}$).³⁴ In the case of LLNOF(-L1), Li rearrangement at a similar intermediate range is low because Li-Li repulsion effect is weaker due to the structure’s intrinsically larger Li-Li site distances ($16d$ -to- $16d$: $\sim 3.69 \text{ \AA}$).

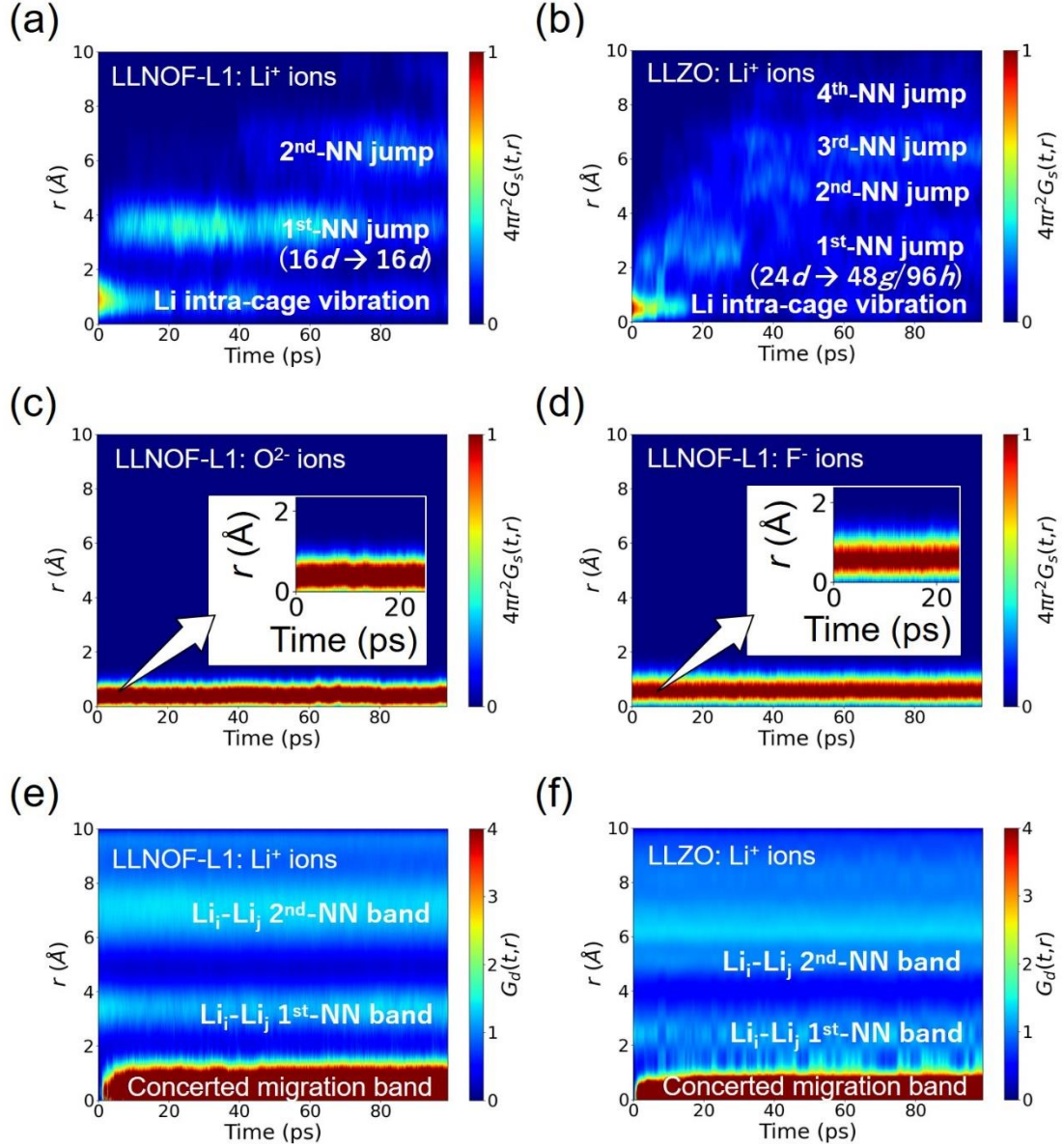


Figure 6. Heatmap profiles for the self (G_s) and distinct (G_d) part of the space-time correlation (van Hove) function derived from 1000-K NVT-MD trajectories: (a) G_s for Li^+ ions in LLNOF-L1 structure, (b) G_s for Li^+ ions in cubic LLZO structure, (c) G_s for O^{2-} ions in LLNOF-L1 structure, (d) G_s for F^- ions in LLNOF-L1 structure, (e) G_d for Li^+ ions in LLNOF-L1 structure, and (f) G_d for Li^+ ions in cubic LLZO structure.

Low-energy optical phonon has been previously reported to play a role on superionic conduction, as reflected in the observed positive (negative) correlation between phonon amplitudes and σ_{Li} (E_a) for many ionic conductors.⁴⁹⁻⁵¹ To study this property, the atom-projected phonon density of states (DOS) of LLNOF-L1 is calculated from the 1000-K MD data; the phonon DOS data for LLZO is also

calculated for comparison.

In LLNOF-L1, Li, La, Nb, O, and F atoms have phonon DOS contributions in energy ranges of $0 < \hbar\omega < 80$ meV, $0 < \hbar\omega < 30$ meV, $0 < \hbar\omega < 80$ meV, $0 < \hbar\omega < 120$ meV, and $0 < \hbar\omega < 60$ meV, respectively (Fig. 7a). Corresponding phonon band center (c_{ph})⁵² positions are located at ~27 meV, ~11 meV, ~21 meV, ~43 meV, and ~22 meV, respectively. Here, the large vibrational amplitudes ($\hbar\omega < 10$ meV) can be mainly ascribed to the relatively heavier atoms (La and Nb). Near this low-energy regime ($\hbar\omega < 20$ meV), O, F and Li atoms also have significant contributions. The F phonon states appear in a narrower energy range and a lower c_{ph} position than the O phonon states, this is consistent with the larger vibration of F atoms than O atoms that is registered in the G_s plot (Fig. 6c, 6d). The F- c_{ph} position is also found to be closer to the Li- c_{ph} position. Li atoms interacts electrostatically with O and F atoms (as a LiO_6F_2 unit), thereby explaining their vibrational states at the lower half of the phonon DOS spectrum. However, O atoms also interacts with Nb atoms (as NbO_6 unit) which have vibrational states at the intermediate energy range ($20 < \hbar\omega < 60$ meV), resulting to the O- c_{ph} position to be located at a higher phonon energy relative to F- c_{ph} position.

In the case of LLZO, Li, La, Zr, and O atoms have contributions in energy ranges of $0 < \hbar\omega < 100$ meV, $0 < \hbar\omega < 30$ meV, $0 < \hbar\omega < 60$ meV, and $0 < \hbar\omega < 100$ meV; corresponding c_{ph} positions are located at ~49 meV, ~14 meV, ~22 meV, and ~44 meV, respectively (Fig. 7b). The La- and O- c_{ph} positions in LLZO and LLNOF-L1 are similar, but more O phonon states appear at $\hbar\omega < 20$ meV for the latter. Another difference is that the Li- c_{ph} position for LLZO (~49 meV) is significantly higher than for LLNOF-L1 (~27 meV), this means that Li atoms in the latter have a larger vibrational amplitude and more significant translational motion on the average. This finding agrees well with the abovementioned inverse relationship between Li vibrational amplitude and E_a ; AIMD-based E_a values for LLNOF-L1 and LLZO are 0.21 and 0.33 eV³⁴, respectively. As previously pointed out, the larger geometric “free space” provided by the hexagonal tunnels in LLNOF may have partly induced the characteristically low phonon energies (i.e., larger vibrations) by F, O and Li atoms.

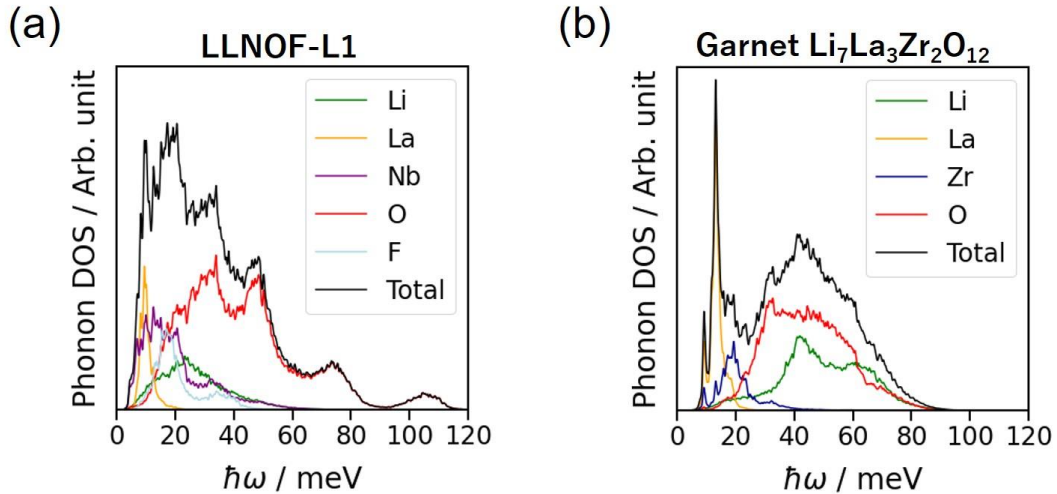


Figure 7. Phonon density of states by NVT-AIMD calculations at 1000 K: (a) pyrochlore $\text{Li}_{1.3125}\text{La}_{0.5625}\text{Nb}_2\text{O}_6\text{F}$ with the L1 structure (LLNOF-L1, see Figure 2c) and (b) garnet cubic $\text{Li}_7\text{La}_3\text{Zr}_2\text{O}_{12}$.

Discussion

LLNOF is predicted to be a metastable phase that can assume various energetically comparable Li/La/Vac ordering configurations. This structure entropy should be taken into account during synthesis so that optimal Li diffusion properties can be achieved. Structurally, the degree of ordering at the 16d site can be classified based on the number of La-free or La-blocked tunnels. The LLNOF structure is expected to become more ordered as the number of La-free tunnels increases. Oppositely, the higher the number of La-blocked tunnels and the number of La cations per tunnel, the more disordered the structure should become. The extent of this La-blocking effect is also expected to be composition-dependent with respect to Li/La content. SEs that demonstrate high σ_{Li} often have crystal structures that have a high degree of disordering in its cation and/or anion sublattices. The ordering-dependent variability on σ_{Li} for LLNOF is partly supported by the present AIMD results (i.e., LLNOF-L1 vs. LLNOF-M1, Fig. 4b). Cubic LLZO also has an intrinsic structure disordering, in relation to its partially occupied Li Wyckoff sites. Another oxide-type SE that shows a similar structural entropy is the perovskite-type $\text{Li}_{3x}\text{La}_{2/3-x}\text{TiO}_3$ (LLTO), in which σ_{Li} is often studied in relation to the presence of Li/La-poor/rich layers within the perovskite structure.⁵³⁻⁵⁴ In LLTO, the subtle distortions brought upon by the complex ordering patterns has been shown to give rise to variability in structure symmetry and σ_{Li} .⁵⁵⁻⁵⁶

A kinetically stabilized LLNOF is predicted to have a poor electrochemical stability, based on the DFT-predicted narrow stability voltage window (2.49 – 3.92 V, Fig. 3a). However, being a metastable phase, the decomposition product phases of LLNOF may extend its stability voltage window (i.e., interphase-controlled electrochemical stability). Specifically, LiF, which is one of the possible decomposition products, can serve as a good interphase layer (0 – 6.36 V window, Fig. 3c). LiF has been used already to improve the cycling performance of conventional Li-ion battery and ASSB cells.⁵⁷⁻⁶¹ LiF has also been reported to be an effective sintering aid, improving the total σ_{Li} of pelletized SE samples.⁶²⁻⁶³ However, it may also have a detrimental effect to battery rate capability because of its intrinsically low Li^+ ion diffusivity.⁶⁴ This tradeoff has to be taken into account in the rational design of an ASSB cell with LLNOF as the SE component.

Based on the findings from AIMD calculations, the Li superionic conductivity of LLNOF may be explained by the following factors: i) the strong concerted migration of Li^+ ions, ii) the large hexagonal tunnels formed by the NbO_6 units which result to an effectively large Li pathway channels that have large site-to-site Li jump distances and less-restricted Li path bottleneck (and therefore lower E_a), and

iii) the relatively large vibrational amplitude of Li atoms which may have been induced by the F atoms through electrostatic interactions (phonon states for F atoms are located in a narrower energy range at the low-energy regime, as compared to O atoms). The relationship between Li vibrational amplitude and σ_{Li} (E_a) has been confirmed by phonon DOS analysis. Intrinsic defects can also significantly affect the σ_{Li} of LLNOF. For example, the LiF Schottky defect causes a ~ 2 orders of magnitude drop in σ_{Li} . This can be explained by two reasons: decreased concentration of Li^+ ion charge carriers and changes in local Li diffusion behavior around F vacancies, noting that the large vibration amplitude of F atoms is strongly correlated with the large vibrational amplitude of Li atoms.

A comprehensive comparison between LLNOF and other known SEs is performed with respect to phase stability (thermodynamic decomposition energy, E_D), electronic band gap energy (E_g), electrochemical stability (decomposition-related voltage stability window), chemical stability (air stability) and ionic conductivity. The actual values are listed in Table 3. Most of the SEs, including LLNOF, are determined to be metastable phases based on DFT-calculated E_d (> 0). The garnet LLZO and Li_3YBr_6 SEs show the highest E_g values of 4.10 and 4.14 eV, respectively, while sulfide-type SEs generally have $E_g < 3$ eV. The relatively smaller E_g of the latter can be explained by the weaker chemical bonding strength between cations and S^{2-} anions as compared to O^{2-} anions in oxide-type electrolytes. In the case of LLNOF(-L1), it has a similar E_g value as with sulfide-type electrolytes, this owed to the relatively low reductive stability of Nb^{5+} , which is consistent with the energetically low-lying Nb 4d states in the conduction band minimum as suggested by its DFT electronic density of states (see Fig. S7). Both LLNOF and LATP contain transition metal (Nb and Ti, respectively) which can be reduced at the low voltage regime, thereby explaining their relatively poor reductive stability. Although LLZO is shown to be relatively more stable reductively (0.05 V), it still can be reduced when in contact with a pure Li metal anode (0 V), this is consistent with the experimental findings. Meanwhile, the air stability of SEs is often investigated under moisture-contact condition. This moisture reactivity can be explained based on hard-soft acid-base (HSAB) theory (i.e., hard-acid species prefer to form strong chemical bonds with hard-base species, while soft-acid species prefer to form bonds with soft-base species).⁶⁵ For example, S (a soft base) in Li_3PS_4 electrolyte is favored to be replaced by O (a hard base) from H_2O molecule to form a strong chemical bond with P (hard acid). In the case of LLNOF, since O forms the anion sublattice, there is no large driving force for forming new chemical bonds when in contact with H_2O ; the high air stability of LLNOF with moisture was also experimentally reported (Ref. 12). On the other hand, sulfide-type SEs are known to suffer from decomposition and toxic H_2S gas formation. In terms of conductivity, sulfide-type (e.g., Argyrodite $\text{Li}_6\text{PS}_5\text{Cl}$, $\text{Li}_{10}\text{GeP}_2\text{S}_{12}$, $\text{Li}_{9.54}\text{Si}_{1.74}\text{P}_{1.44}\text{S}_{11.4}\text{Cl}_{0.3}\text{O}_{0.3}$) as well as halide-type SEs (e.g., Li_3YBr_6) demonstrate an order of 10^{-3} S/cm (or higher), this order of magnitude in conductivity is necessary to achieve low-impedance solid-state cells.⁶⁶ Comparatively, LLNOF also reaches this order of magnitude in conductivity. Both the high conductivity and high air stability of LLNOF makes it a

very promising electrolyte for practical application.

Aside from tuning the Li/La content, it is also worthwhile to explore other cation dopant types for the further optimization of σ_{Li} in LLNOF to reach the practical SE conductivity requirement which is 10^{-2} S/cm order of magnitude.¹¹ For example, substitution at the Nb⁵⁺ site by d^0 cations (e.g., Ti⁴⁺, Zr⁴⁺, Hf⁴⁺)⁶⁷, which can accommodate various local distortion modes and distortion degrees, may further improve σ_{Li} through geometric modulation of the Li pathway channels, tuning of vacancy concentration and maximization of structure entropy (via Li/La/Vac disordering).

Table 3. Comparison of important battery-related properties of different all-solid-state battery electrolytes.

Composition	DFT decomposition energy (E_d) / meV/atom*	Electronic band gap energy (E_g) / eV*	Voltage stability window / V (vs. Li ⁺ /Li)*	Air stability vs. H ₂ O**	Ionic conductivity / 10^{-3} S/cm*,**
LLNOF-L1	31	2.76	2.49 – 3.92 (this work)	-	1.07 (bulk, this work)
Li _{1.25} La _{0.58} Nb ₂ O ₆ F	-	-	-	High ¹²	3.9 ¹²
Cubic Li ₇ La ₃ Zr ₂ O ₁₂ (LLZO)	18	4.10	0.05 – 2.90 (this work)	High ⁶⁸	0.11 ³⁴
Argyrodite Li ₆ PS ₅ Cl	21	1.98	1.71 – 2.01 ²¹	Low ⁶⁹	1.33 ³⁵
Li ₃ YBr ₆	26	4.14	0.59 – 0 3.15 ⁷⁰	High ⁷¹	1.7 ³⁶

$\text{Li}_{1.3}\text{Al}_{0.3}\text{Ti}_{1.7}(\text{PO}_4)_3$ (LATP)	29	2.60	2.17 – 4.21 ²¹	High ⁷²	0.7 ³⁷
Li_3PS_4	0	2.70	1.71 – 2.31 ²¹	Low ⁶⁵	0.16 ⁷³
$\text{Li}_{10}\text{GeP}_2\text{S}_{12}$	21	2.20	1.71 – 2.14 ²¹	Low ⁶⁵	12 ³⁸
$\text{Li}_{9.54}\text{Si}_{1.74}\text{P}_{1.44}\text{S}_{11.4}\text{Cl}_{0.3}\text{O}_{0.3}$	-		-	Low ⁶⁵	28 ³⁹

*DFT result, **Experimental data.

Conclusions

In this work, the crystal structure, phase stability, electrochemical stability, and Li^+ ion transport property of LLNOF SE was systematically investigated by DFT and AIMD calculations. The crystal structure of LLNOF is comprised with hexagonal tunnels formed by corner-sharing NbO_6 octahedral units and with $\text{Li/LaO}_6\text{F}_2$ pseudo-rhombohedral units residing within the tunnels. Depending on the Li/La/Vac arrangement, the tunnels can be described as either La-free or La-blocked. LLNOF is predicted to be a metastable phase with an interphase-controlled electrochemical window. The La positions ultimately determines the Li pathway channel and topology, which has ~72% percolated Li^+ at the investigated composition ($\text{Li}_{1.3125}\text{La}_{0.5625}\text{Nb}_2\text{O}_6\text{F}$). AIMD calculations show the same order of magnitude for the bulk Li ion⁺ conductivity vs. experiment (10^{-3} S/cm). The Li^+ ion conduction mechanism in LLNOF was determined to proceed via a concerted migration process. Li ion dynamics analysis by van Hove correlation approach, as well as phonon DOS analysis, have revealed the relatively larger vibrational amplitude of F atoms as compared to O atoms in the LLNOF structure. This can explain the low phonon band center position of Li atoms which correlates well with the observed Li superionic conductivity of LLNOF.

Acknowledgments

RJ is thankful for the support in part by JSPS KAKENHI grant number JP21K14729, by MEXT as Materials Processing Science project (“Materealize”) grant number JPMXP0219207397, as well as JST through Green Technologies of Excellence (GteX) grant number JPMJGX23S2. The calculations were performed on the supercomputers at NIMS (Numerical Materials Simulator) and the

supercomputer Fugaku at the RIKEN through the HPCI System Research Project (project ID: hp240118, hp210105). Crystal structures were visualized using the VESTA software.⁷⁴ The python library Matplotlib was used for drawing the plots.⁷⁵

References

1. Takada, K., Progress in solid electrolytes toward realizing solid-state lithium batteries. *J Power Sources* **2018**, *394*, 74-85.
2. Janek, J.; Zeier, W. G., A solid future for battery development. *Nat Energy* **2016**, *1*.
3. Manthiram, A.; Yu, X. W.; Wang, S. F., Lithium battery chemistries enabled by solid-state electrolytes. *Nat Rev Mater* **2017**, *2* (4).
4. Kimura, T.; Inaoka, T.; Izawa, R.; Nakano, T.; Hotehama, C.; Sakuda, A.; Tatsumisago, M.; Hayashi, A., Stabilizing High-Temperature α -Li₃PS₄ by Rapidly Heating the Glass. *J Am Chem Soc* **2023**, *145* (26), 14466-14474.
5. Kato, Y.; Hori, S.; Saito, T.; Suzuki, K.; Hirayama, M.; Mitsui, A.; Yonemura, M.; Iba, H.; Kanno, R., High-power all-solid-state batteries using sulfide superionic conductors. *Nat Energy* **2016**, *1*.
6. Muramatsu, H.; Hayashi, A.; Ohtomo, T.; Hama, S.; Tatsumisago, M., Structural change of Li₂S-P₂S₅ sulfide solid electrolytes in the atmosphere. *Solid State Ionics* **2011**, *182* (1), 116-119.
7. Murugan, R.; Thangadurai, V.; Weppner, W., Fast lithium ion conduction in garnet-type Li₇La₃Zr₂O₁₂. *Angew Chem Int Edit* **2007**, *46* (41), 7778-7781.
8. O'Callaghan, M. P.; Cussen, E. J., Lithium dimer formation in the Li-conducting garnets Li_{5+x}Ba_xLa_{3-x}Ta₂O₁₂ (0 < x ≤ 1.6). *Chem Commun* **2007**, (20), 2048-2050.
9. Ramakumar, S.; Deviannapoorani, C.; Dhivya, L.; Shankar, L. S.; Murugan, R., Lithium garnets: Synthesis, structure, Li⁺ conductivity, Li⁺ dynamics and applications. *Prog Mater Sci* **2017**, *88*, 325-411.
10. Li, Y. T.; Han, J. T.; Wang, C. A.; Xie, H.; Goodenough, J. B., Optimizing Li⁺ conductivity in a garnet framework. *J Mater Chem* **2012**, *22* (30), 15357-15361.
11. Randau, S.; Weber, D. A.; Kotz, O.; Koerver, R.; Braun, P.; Weber, A.; Ivers-Tiffée, E.; Adermann, T.; Kulisch, J.; Zeier, W. G.; Richter, F. H.; Janek, J., Benchmarking the performance of all-solid-state lithium batteries. *Nat Energy* **2020**, *5* (3), 259-270.
12. Aimi, A.; Onodera, H.; Shimonishi, Y.; Fujimoto, K.; Yoshida, S., High Li-Ion Conductivity in Pyrochlore-Type Solid Electrolyte Li_{2-x}La_{(1+x)/3}M₂O₆F (M = Nb, Ta). *Chem Mater* **2024**.
13. Galven, C.; Legein, C.; Body, M.; Fourquet, J. L.; Buzaré, J. Y.; Le Berre, F.; Crosnier-Lopez, M. P., New Oxyfluoride Pyrochlores Li_{2-x}La_{(1+x)/3}□_{(2x-1)/3}B₂O₆F (B = Nb, Ta): Average and Local Structure Characterization by XRD, TEM and F Solid-State NMR Spectroscopy. *Eur J Inorg Chem* **2010**, (33), 5272-5283.
14. Kresse, G., Ab-Initio Molecular-Dynamics for Liquid-Metals. *J Non-Cryst Solids* **1995**, *193*,

222-229.

15. Kresse, G.; Furthmüller, J., Efficient iterative schemes for ab initio total-energy calculations using a plane-wave basis set. *Phys Rev B* **1996**, *54* (16), 11169-11186.
16. Ong, S. P.; Richards, W. D.; Jain, A.; Hautier, G.; Kocher, M.; Cholia, S.; Gunter, D.; Chevrier, V. L.; Persson, K. A.; Ceder, G., Python Materials Genomics (pymatgen): A robust, open-source python library for materials analysis. *Comp Mater Sci* **2013**, *68*, 314-319.
17. Monkhorst, H. J.; Pack, J. D., Special Points for Brillouin-Zone Integrations. *Phys Rev B* **1976**, *13* (12), 5188-5192.
18. Ong, S. P.; Wang, L.; Kang, B.; Ceder, G., Li-Fe-P-O₂ phase diagram from first principles calculations. *Chem Mater* **2008**, *20* (5), 1798-1807.
19. Bergerhoff, G.; Berndt, M., Inorganic Structural Chemistry with Crystallographic Databases. *Acta Crystallographica a-Foundation and Advances* **1996**, *52*, C314-C314.
20. Jain, A.; Ong, S. P.; Hautier, G.; Chen, W.; Richards, W. D.; Dacek, S.; Cholia, S.; Gunter, D.; Skinner, D.; Ceder, G.; Persson, K. A., Commentary: The Materials Project: A materials genome approach to accelerating materials innovation. *Apl Mater* **2013**, *1* (1).
21. Zhu, Y. Z.; He, X. F.; Mo, Y. F., Origin of Outstanding Stability in the Lithium Solid Electrolyte Materials: Insights from Thermodynamic Analyses Based on First-Principles Calculations. *Acs Appl Mater Inter* **2015**, *7* (42), 23685-23693.
22. Hoover, W. G.; Ladd, A. J. C.; Moran, B., High-Strain-Rate Plastic-Flow Studied Via Non-Equilibrium Molecular-Dynamics. *Phys Rev Lett* **1982**, *48* (26), 1818-1820.
23. Nose, S., A Unified Formulation of the Constant Temperature Molecular-Dynamics Methods. *J Chem Phys* **1984**, *81* (1), 511-519.
24. He, Y.; Burov, S.; Metzler, R.; Barkai, E., Random time-scale invariant diffusion and transport coefficients. *Phys Rev Lett* **2008**, *101* (5).
25. Atkins, P., *Atkins' Physical Chemistry*. 11 ed.; Oxford University Press: 2006; p 1040.
26. Nitzan, A., *Chemical Dynamics in Condensed Phases: Relaxation, Transfer and Reactions in Condensed Molecular Systems*. Oxford Graduate Texts; Oxford University Press: Oxford: 2006.
27. Vanhove, L., Correlations in Space and Time and Born Approximation Scattering in Systems of Interacting Particles. *Phys Rev* **1954**, *95* (1), 249-262.
28. Harada, Y.; Hirakoso, Y.; Kawai, H.; Kuwano, J., Order-disorder of the A-site ions and lithium ion conductivity in the perovskite solid solution La_{0.67-x}Li_{3x}TiO₃ (x=0.11). *Solid State Ionics* **1999**, *121* (1-4), 245-251.
29. Sun, W. H.; Dacek, S. T.; Ong, S. P.; Hautier, G.; Jain, A.; Richards, W. D.; Gamst, A. C.; Persson, K. A.; Ceder, G., The thermodynamic scale of inorganic crystalline metastability. *Sci Adv* **2016**, *2* (11).
30. Li, Y. J.; Chen, B.; Wang, Y. P.; Xing, H.; Zhao, W.; Zhang, G.; Shi, S. Q., Inhibiting Dendrite Growth by Customizing Electrolyte or Separator to Achieve Anisotropic Lithium-Ion Transport: A Phase-

Field Study. *Acta Phys-Chim Sin* **2024**, *40* (3).

31. Jian, Z. L.; Lu, X.; Fang, Z.; Hu, Y. S.; Zhou, J.; Chen, W.; Chen, L. Q., LiNb₃O₈ as a novel anode material for lithium-ion batteries. *Electrochem Commun* **2011**, *13* (10), 1127-1130.
32. Wolfenstine, J.; Allen, J. L.; Read, J.; Sakamoto, J., Chemical stability of cubic Li₇La₃Zr₂O₁₂ with molten lithium at elevated temperature. *J Mater Sci* **2013**, *48* (17), 5846-5851.
33. Konishi, S.; Ohno, H., Conductivity Measurement and Effect of Impurity Ions Dissolved in Li₂O. *J Nucl Mater* **1988**, *152* (1), 9-13.
34. Jalem, R.; Yamamoto, Y.; Shiiba, H.; Nakayama, M.; Munakata, H.; Kasuga, T.; Kanamura, K., Concerted Migration Mechanism in the Li Ion Dynamics of Garnet-Type Li₇La₃Zr₂O₁₂. *Chem Mater* **2013**, *25* (3), 425-430.
35. Boulineau, S.; Courty, M.; Tarascon, J. M.; Viallet, V., Mechanochemical synthesis of Li-argyrodite Li₆PS₅X (= Cl, Br, I) as sulfur-based solid electrolytes for all solid state batteries application. *Solid State Ionics* **2012**, *221*, 1-5.
36. Asano, T.; Sakai, A.; Ouchi, S.; Sakaida, M.; Miyazaki, A.; Hasegawa, S., Solid Halide Electrolytes with High Lithium-Ion Conductivity for Application in 4 V Class Bulk-Type All-Solid-State Batteries. *Adv Mater* **2018**, *30* (44).
37. Aono, H.; Sugimoto, E.; Sadaoka, Y.; Imanaka, N.; Adachi, G. Y., Ionic-Conductivity of the Lithium Titanium Phosphate (Li_{1+x}M_xTi_{2-x}(PO₄)₃, M = Al, Sc, Y, and La) Systems. *J Electrochem Soc* **1989**, *136* (2), 590-591.
38. Kamaya, N.; Homma, K.; Yamakawa, Y.; Hirayama, M.; Kanno, R.; Yonemura, M.; Kamiyama, T.; Kato, Y.; Hama, S.; Kawamoto, K.; Mitsui, A., A lithium superionic conductor. *Nat Mater* **2011**, *10* (9), 682-686.
39. Li, Y. X.; Daikuhara, S.; Hori, S.; Sun, X. Y.; Suzuki, K.; Hirayama, M.; Kanno, R., Oxygen Substitution for Li-Si-P-S-Cl Solid Electrolytes toward Purified Li₁₀GeP₂S₁₂-Type Phase with Enhanced Electrochemical Stabilities for All-Solid-State Batteries. *Chem Mater* **2020**, *32* (20), 8860-8867.
40. Stauffer, D., Scaling Theory of Percolation Clusters. *Phys Rep* **1979**, *54* (1), 1-74.
41. Jalem, R.; Rushton, M. J. D.; Manalastas, W.; Nakayama, M.; Kasuga, T.; Kilner, J. A.; Grimes, R. W., Effects of Gallium Doping in Garnet-Type Li₇La₃Zr₂O₁₂ Solid Electrolytes. *Chem Mater* **2015**, *27* (8), 2821-2831.
42. He, B.; Mi, P. H.; Ye, A. J.; Chi, S. T.; Jiao, Y.; Zhang, L. W.; Pu, B. W.; Zou, Z. Y.; Zhang, W. Q.; Avdeev, M.; Adams, S.; Zhao, J. T.; Shi, S. Q., A highly efficient and informative method to identify ion transport networks in fast ion conductors. *Acta Mater* **2021**, *203*.
43. Zhang, L. W.; He, B.; Zhao, Q.; Zou, Z. Y.; Chi, S. T.; Mi, P. H.; Ye, A. J.; Li, Y. J.; Wang, D.; Avdeev, M.; Adams, S.; Shi, S. Q., A Database of Ionic Transport Characteristics for Over 29 000 Inorganic Compounds. *Adv Funct Mater* **2020**, *30* (35).
44. Pan, L.; Zhang, L. W.; Ye, A. J.; Chi, S. T.; Zou, Z. Y.; He, B.; Chen, L. L.; Zhao, Q.; Wang, D.;

Shi, S. Q., Revisiting the ionic diffusion mechanism in Li_3PS_4 via the joint usage of geometrical analysis and bond valence method. *J Materiomics* **2019**, 5 (4), 688-695.

45. He, B.; Ye, A. J.; Chi, S. T.; Mi, P. H.; Ran, Y. B.; Zhang, L. W.; Zou, X. X.; Pu, B. W.; Zhao, Q.; Zou, Z. Y.; Wang, D.; Zhang, W. Q.; Zhao, J. T.; Avdeev, M.; Shi, S. Q., CAVD, towards better characterization of void space for ionic transport analysis. *Sci Data* **2020**, 7 (1).

46. He, B.; Chi, S. T.; Ye, A. J.; Mi, P. H.; Zhang, L. W.; Pu, B. W.; Zou, Z. Y.; Ran, Y. B.; Zhao, Q.; Wang, D.; Zhang, W. Q.; Zhao, J. T.; Adams, S.; Avdeev, M.; Shi, S. Q., High-throughput screening platform for solid electrolytes combining hierarchical ion-transport prediction algorithms. *Sci Data* **2020**, 7 (1).

47. Willems, T. F.; Rycroft, C.; Kazi, M.; Meza, J. C.; Haranczyk, M., Algorithms and tools for high-throughput geometry-based analysis of crystalline porous materials. *Micropor Mesopor Mat* **2012**, 149 (1), 134-141.

48. Adams, S.; Rao, R. P., Ion transport and phase transition in $\text{Li}_{7-x}\text{La}_3(\text{Zr}_{2-x}\text{M}_x)\text{O}_{12}$ ($\text{M} = \text{Ta}^{5+}, \text{Nb}^{5+}$, $x=0, 0.25$). *J Mater Chem* **2012**, 22 (4), 1426-1434.

49. Wakamura, K., Roles of phonon amplitude and low-energy optical phonons on superionic conduction. *Phys Rev B* **1997**, 56 (18), 11593-11599.

50. Kraft, M. A.; Culver, S. P.; Calderon, M.; Böcher, F.; Krauskopf, T.; Senyshyn, A.; Dietrich, C.; Zevalkink, A.; Janek, J.; Zeier, W. G., Influence of Lattice Polarizability on the Ionic Conductivity in the Lithium Superionic Argyrodites $\text{Li}_6\text{PS}_5\text{X}$ ($\text{X} = \text{Cl}, \text{Br}, \text{I}$). *J Am Chem Soc* **2017**, 139 (31), 10909-10918.

51. Krauskopf, T.; Pompe, C.; Kraft, M. A.; Zeier, W. G., Influence of Lattice Dynamics on Na^+ Transport in the Solid Electrolyte $\text{Na}_3\text{PS}_{4-x}\text{Se}_x$. *Chem Mater* **2017**, 29 (20), 8859-8869.

52. Muy, S.; Bachman, J. C.; Giordano, L.; Chang, H. H.; Abernathy, D. L.; Bansal, D.; Delaire, O.; Hori, S.; Kanno, R.; Maglia, F.; Lupart, S.; Lamp, P.; Shao-Horn, Y., Tuning mobility and stability of lithium ion conductors based on lattice dynamics. *Energ Environ Sci* **2018**, 11 (4), 850-859.

53. Inaguma, Y.; Chen, L. Q.; Itoh, M.; Nakamura, T.; Uchida, T.; Ikuta, H.; Wakihara, M., High Ionic-Conductivity in Lithium Lanthanum Titanate. *Solid State Commun* **1993**, 86 (10), 689-693.

54. Gao, X.; Fisher, C. A. J.; Kimura, T.; Ikuhara, Y. H.; Moriwake, H.; Kuwabara, A.; Oki, H.; Tojigamori, T.; Huang, R.; Ikuhara, Y., Lithium Atom and A-Site Vacancy Distributions in Lanthanum Lithium Titanate. *Chem Mater* **2013**, 25 (9), 1607-1614.

55. Stramare, S.; Thangadurai, V.; Weppner, W., Lithium lanthanum titanates: A review. *Chem Mater* **2003**, 15 (21), 3974-3990.

56. Yashima, M.; Itoh, M.; Inaguma, Y.; Morii, Y., Crystal structure and diffusion path in the fast lithium-ion conductor $\text{La}_{0.62}\text{Li}_{0.16}\text{TiO}_3$. *J Am Chem Soc* **2005**, 127 (10), 3491-3495.

57. Xiao, Z. Y.; Zhu, X. B.; Wang, S. G.; Shi, Y. H.; Zhang, H. M.; Xu, B. B.; Zhao, C. F.; Zhao, Y., Construction of Uniform LiF Coating Layers for Stable High-Voltage LiCoO_2 Cathodes in Lithium-Ion Batteries. *Molecules* **2024**, 29 (6).

58. Zhao, T. L.; Li, L.; Chen, R. J.; Wu, H. M.; Zhang, X. X.; Chen, S.; Xie, M.; Wu, F.; Lu, J.;

- Amine, K., Design of surface protective layer of LiF/FeF₃ nanoparticles in Li-rich cathode for high-capacity Li-ion batteries. *Nano Energy* **2015**, *15*, 164-176.
59. Du, J. M.; Wang, W. Y.; Eng, A. Y. S.; Liu, X. X.; Wan, M. T.; Seh, Z. W.; Sun, Y. M., Metal/LiF/Li₂O Nanocomposite for Battery Cathode Prelithiation: Trade-off between Capacity and Stability. *Nano Lett* **2020**, *20* (1), 546-552.
 60. Li, Y. X.; Li, Y. Q.; Yang, Y. N.; Cui, Z. H.; Wang, J. C.; Zhang, T., Conversion inorganic interlayer of a LiF/graphene composite in all-solid-state lithium batteries. *Chem Commun* **2020**, *56* (11), 1725-1728.
 61. Shi, X.; Pang, Y.; Wang, B.; Sun, H.; Wang, X.; Li, Y.; Yang, J.; Li, H. W.; Zheng, S., In situ forming LiF nanodecorated electrolyte/electrode interfaces for stable all-solid-state batteries. *Mater Today Nano* **2020**, *10*.
 62. Yao, Z. R.; Zhu, K. J.; Zhang, J.; Li, J.; Li, X.; Wang, J.; Yan, K.; Liu, J. S., LiF-Assisted Synthesis of Perovskite-Type Li_{0.35}La_{0.55}TiO₃ Solid Electrolyte for Rechargeable Lithium-Metal Batteries. *J Electron Mater* **2022**, *51* (2), 736-744.
 63. Xiong, L. L.; Ren, Z. H.; Xu, Y. L.; Mao, S. C.; Lei, P.; Sun, M. T., LiF assisted synthesis of LiTi₂(PO₄)₃ solid electrolyte with enhanced ionic conductivity. *Solid State Ionics* **2017**, *309*, 22-26.
 64. Maier, J., Defect Chemistry - Composition, Transport, and Reactions in the Solid-State .1. Thermodynamics. *Angewandte Chemie-International Edition in English* **1993**, *32* (3), 313-335.
 65. Lu, P. S.; Wu, D. X.; Chen, L. Q.; Li, H.; Wu, F., Air Stability of Solid-State Sulfide Batteries and Electrolytes. *Electrochem Energy R* **2022**, *5* (3).
 66. Chen, S.; Yu, C.; Luo, Q. Y.; Wei, C. C.; Li, L. P.; Li, G. S.; Cheng, S. J.; Xie, J., Research Progress of Lithium Metal Halide Solid Electrolytes. *Acta Phys-Chim Sin* **2023**, *39* (8).
 67. Urban, A.; Abdellahi, A.; Dacek, S.; Artrith, N.; Ceder, G., Electronic-Structure Origin of Cation Disorder in Transition-Metal Oxides. *Phys Rev Lett* **2017**, *119* (17).
 68. Hofstetter, K.; Samson, A. J.; Narayanan, S.; Thangadurai, V., Present understanding of the stability of Li-stuffed garnets with moisture, carbon dioxide, and metallic lithium. *J Power Sources* **2018**, *390*, 297-312.
 69. Seol, K.; Kaliyaperumal, C.; Uthayakumar, A.; Yoon, I.; Lee, G. H. Y.; Shin, D., Enhancing the Moisture Stability and Electrochemical Performances of Li₆PS₅Cl Solid Electrolytes through Ga Substitution. *Electrochim Acta* **2023**, *441*.
 70. Wang, S.; Bai, Q.; Nolan, A. M.; Liu, Y. S.; Gong, S.; Sun, Q.; Mo, Y. F., Lithium Chlorides and Bromides as Promising Solid-State Chemistries for Fast Ion Conductors with Good Electrochemical Stability. *Angew Chem Int Edit* **2019**, *58* (24), 8039-8043.
 71. Tao, B. R.; Zhong, D. L.; Li, H. D.; Wang, G. F.; Chang, H. X., Halide solid-state electrolytes for all-solid-state batteries: structural design, synthesis, environmental stability, interface optimization and challenges. *Chem Sci* **2023**, *14* (33), 8693-8722.

72. Zhu, J. P.; Zhao, J.; Xiang, Y. X.; Lin, M.; Wang, H. C.; Zheng, B. Z.; He, H. J.; Wu, Q. H.; Huang, J. Y.; Yang, Y., Chemomechanical Failure Mechanism Study in NASICON-Type $\text{Li}_{1.3}\text{Al}_{0.3}\text{Ti}_{1.7}(\text{PO}_4)_3$ Solid-State Lithium Batteries. *Chem Mater* **2020**, 32 (12), 4998-5008.
73. Liu, Z. C.; Fu, W. J.; Payzant, E. A.; Yu, X.; Wu, Z. L.; Dudney, N. J.; Kiggans, J.; Hong, K. L.; Rondinone, A. J.; Liang, C. D., Anomalous High Ionic Conductivity of Nanoporous $\beta\text{-Li}_3\text{PS}_4$. *J Am Chem Soc* **2013**, 135 (3), 975-978.
74. Momma, K.; Izumi, F., for three-dimensional visualization of crystal, volumetric and morphology data. *J Appl Crystallogr* **2011**, 44, 1272-1276.
75. Hunter, J. D., Matplotlib: A 2D graphics environment. *Comput Sci Eng* **2007**, 9 (3), 90-95.

TOC

